Electric Propulsion Research Activities in the Plasma, Energy, & Space Propulsion Laboratory

IEPC-2025-661

Presented at the 39th International Electric Propulsion Conference Imperial College London • London, United Kingdom 14-19 September 2025

Richard E. Wirz^{1,2}
University of California, Los Angeles, CA, 90095, USA
Oregon State University, Corvallis, OR, 97331, USA

Richard A. Obenchain^{||}, Christoper M. Cretel^{||}, Ryan W. Cowan^{||}, Luke K. Franz^{||}, Ian J. Hofbeck^{||}, Andrea M. Harteloo^{||}, Blake Haist[§], Alexander Reed^{||}, Adael L. Scatena^{||}, John Madland^{||}, Saptarshi Biswas[¶], Mansur Tisaev[¶], Augustus Pendergrass

Oregon State University, Corvallis, OR, 97331, USA

McKenna J. D. Breddan[‡], Mary Konopliv[‡], Patrick Crandall[‡], Graeme Sabiston[‡], Nicolas Rongione[¶], Angelica Ottavio[‡], Ehsan Taghizadeh[‡], Jorge Fernandez-Coppel Velasco[∥], Jaime Marian[¶], *University of California, Los Angeles, CA, 90095, USA*

Shehan Parmar^{||} *Georgia Institute of Technology, Atlanta, GA, 30332, USA*

The Plasma, Energy, & Space Propulsion Laboratory (PESPL) investigates a wide range of topics relevant to space Electric Propulsion (EP) since its inception in 2008 at the University of California, Los Angeles (UCLA) in the United States and continues these topics since its migration from UCLA to Oregon State University (OSU) starting in 2022. In support of NASA's JANUS Institute to investigate facility effects for high-power EP, we have developed high-fidelity neutral ingestion simulations for ion thrusters and reduced order simulations for rapid optimization of vacuum facility design. A new diagnostic for high-speed, non-intrusive thruster and plasma diagnosis, FastOES, has been developed and deployed successfully to measure time-resolved ion, neutral, and electron properties to characterize the predator-prey behavior for coherent Hall thruster breathing modes. Recently, we successfully developed an RF ion thruster for characterizing alternative propellants such as those for air-breathing (ABEP) and other molecular propellants. PESPL efforts in electrospray propulsion have continued, including exploration of plume divergence and "traffic jams", investigation into emission-site physics to understand species populations and dynamics, and fundamental studies of ionic liquids and their emissions and bulk-phase behavior. One area of investigation is the science and technology of plasma material interactions (PMI) where PESPL have performed the first-ever demonstration of a material exhibiting persistent sputtering yield reduction along with the discovery of a new plasma-material regime where the plasma infuses into the material volume. These discoveries are now being used to develop new materials optimized for high energy density plasma applications from EP to fusion applications. Other recent efforts in plasma physics and devices also include high-power hollow cathodes and plasma medicine for COVID-19 and cancer treatment.

[¶] Postdoctoral Scholar



¹ Professor, Mechanical & Aerospace Engineering, wirz@ucla.edu, AIAA Associate Fellow

 $^{^2}$ †Boeing Professor, Executive Director of Aerospace Research Programs, College of Engineering, Richard.Wirz@oregonstate.edu

^{||} Graduate Research Assistant

[‡] Doctoral Graduate

I. Introduction

Electric propulsion research at the Plasma, Energy, & Space Propulsion Laboratory (PESPL) involves wide range of electric propulsion technologies. We explore the physics behind the plasma dynamics, plasma material interactions, and electrohydrodynamics of electric propulsion devices. PESPL was started at UCLA in 2008 and recently moved, with PESPL Director Prof. Wirz, to Oregon State University (OSU) in 2022 as a part of the OSU College of Engineering's initiative to increase graduate-level research in aerospace science and engineering in the State of Oregon, USA. Research activities have continued at UCLA for senior UCLA graduate students. Therefore, this paper covers activities across PESPL at both UCLA and OSU.

II. Electric Propulsion Facilities

A. Facility Effects

As part of the JANUS goals, we are researching several aspects of facility design with the objective of reducing the impact of a facility on thrusters tested therein by using rapid reduced-order models. The Large Vacuum Test Facility (LVTF) at the University of Michigan has been used as a test case for optimizing facility design due to its frequent involvement in testing high power EP devices¹. The effort involved studying the impact of differential pumping on flux to the thruster face during hot flow. An annular place of varying position and central radius was tested at 6 locations within LVFT and compared to the base operational case (Fig. 1); only one test condition had a reduced flux to thruster face for a reduction of approximately 30%. Such rapid testing of multiple configurations can be used to define a target set of improvements that can then be studied with higher fidelity methods.

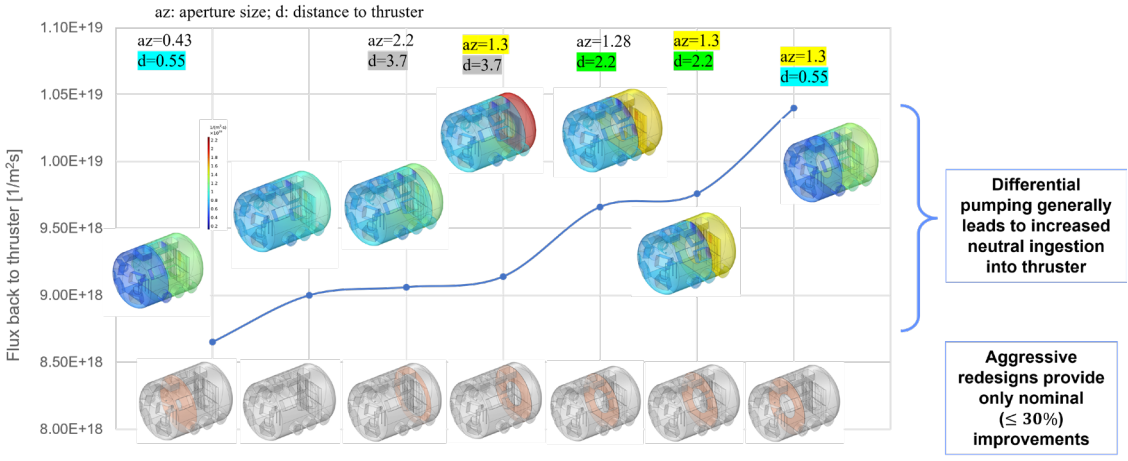


Figure 1. Computational analysis of changes to University of Michigan's Large Vacuum Test Facility (LVTF) by addition of an annular surface of varying position and central aperture. Six test modifications were executed in addition to the base case; all but one test showed increased flux to the thruster face relative to the base case. The remaining test case reduced flux to the thruster face by approximately 30%.

To accurately assess and model the impacts of facility effects during EP testing, the transport of mass and energy within a facility must be well understood. As part of efforts to characterize facilities and quantify neutral-based facility effects, we simulated hot neutral flow within two world-class EP test facilities with identical mass flow and pumping capability². Figure 2(a) shows the six pump configurations used in the two facilities. The resulting flux values to thruster surfaces and several facility surfaces were compared, and an analytical model (Fig. 2(b)) was begun, quantifying neutral flux based on the combination of a characteristic flux describing the experimental steady-state condition and a drift flux describing the experimental mass flow conditions. Comparisons of the resulting fluxes, shown in Fig. 2(c-e), show that similar mass flow conditions can result in different local environments near the thruster and lead to differences in facility effects. Further refinement of the analytical model is underway



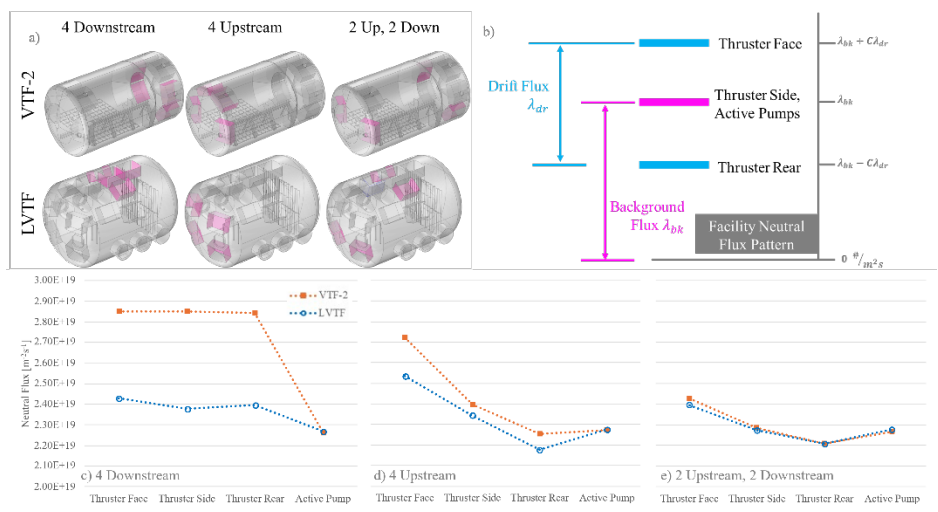


Figure 2. Comparison of neutral flux to thruster surfaces between VTF-2 and LVTF for the three pump conditions: 4 Downstream (A), 4 Upstream (b), and 2 Up 2 Down (c).

Extrapolation from in-facility test results to spacelike conditions requires understanding of the facility effects that are impacting the thruster. As part of a collaboration with Dr. John Foster at the University of Michigan, we investigated the doubles-to-singles ion ratios measured during operation of the NSTAR thruster under three throttle conditions and four pump configurations³. Initial corrections to the CEX rates using standard CEX correction methods failed to predict a common thruster-face exit behavior that would be expected from removal of the facility effect⁴. Using a modified method, we included the effect of CEX interaction with plume neutrals and further reduced the discrepancies between the pressure conditions. The method for extrapolating to a neutral plume density contribution at some distance downstream can be adapted to both Hall effect and gridded ion thrusters and used in similar correction methods, such as those for momentum exchange events

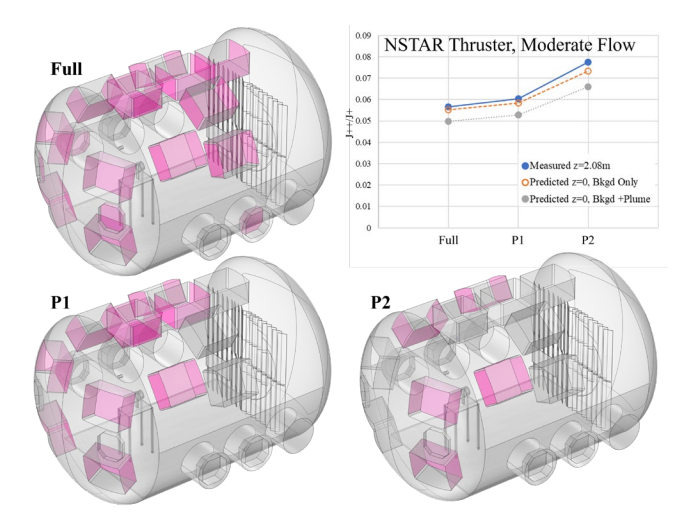


Figure 3. Analysis of neutral particle conditions under three separate pumping configurations and their use in correcting for plume depletion due to CEX events



B. Gridded Ion Thruster Predictive Engineering Models (GIT PEM)

The Gridded Ion Thruster Predictive Engineering Model (GIT PEM) is a reduced-order framework developed under JANUS to evaluate thruster lifetime with quantified uncertainty⁵. It integrates the physics of grid erosion, carbon deposition, and electron backstreaming while remaining computationally efficient enough to support large Monte Carlo ensembles. Equation (1) captures screen grid erosion due to discharge ions crossing the sheath: the Bohm flux is corrected for double-ion contributions and sputter yields, translating plasma conditions directly into erosion rates. By representing these mechanisms analytically rather than through particle tracking, the PEM retains key physics while enabling simulation times on the order of seconds.

$$\Gamma_{Bohm}^{S} = \frac{1}{1+\gamma} \Gamma_{Bohm} [Y(\varepsilon^{+}) + \gamma \sqrt{2} Y(\varepsilon^{++})]$$
(1)

A second life-limiting process, electron backstreaming, is treated with a similarly tractable approach. Equation (2) expresses the backstreaming onset voltage, *Vebs*, in terms of sheath potentials, beamlet space-charge corrections, and plasma parameters. This reduced form emerges after simplifying the full backstreaming current integral and substituting an approximate polynomial potential profile. The analytic treatment captures how grid erosion, beam current density, and electron temperature collectively raise or lower the threshold voltage for suppressing electrons, establishing a practical metric for thruster lifetime without requiring iterative Poisson solutions.

$$V_{ebs} = \phi_{sp} + \Delta V - \frac{c_1 c_2 T_e}{R_{ebs} I_B} \tag{2}$$

The results demonstrate how facility effects can mask true in-space behavior. Figure 4 contrasts GIT PEM predictions with and without facility contributions. Under ground test conditions that include plume charge-exchange ions and carbon redeposition, the model aligns well with Long Duration Test data. When these effects are removed to represent a space-like environment, the predicted V_{ebs} rises significantly, revealing that ground data underestimates erosion-driven voltage increases. This comparison highlights the importance of explicitly modeling facility interactions when extrapolating ground tests to flight conditions, reinforcing the PEM's value as a fast yet physically grounded mission analysis tool.

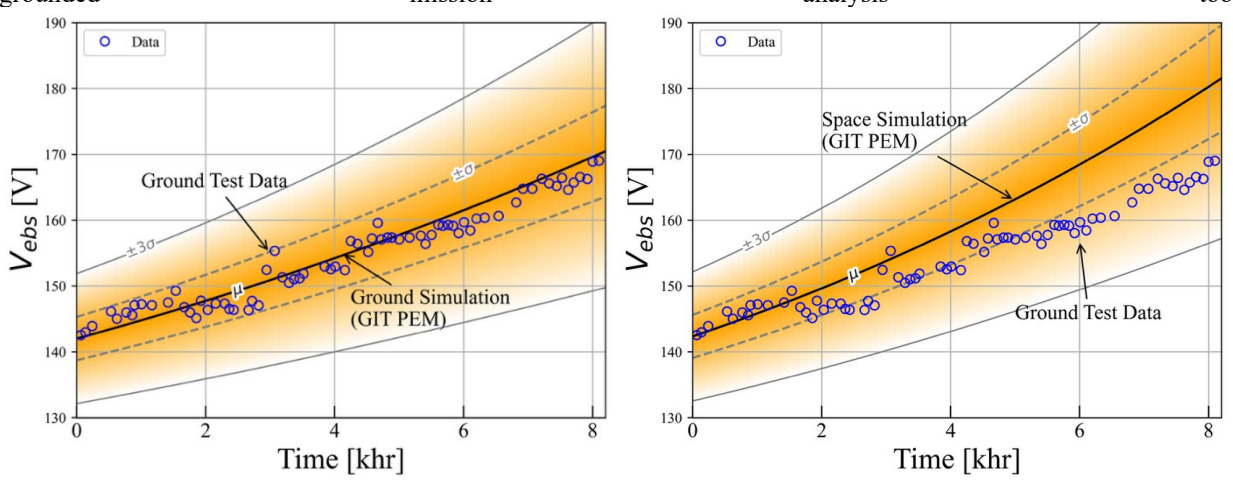


Figure 4. GIT PEM simulating ground testing data and correlating it with LDT measured V_{ebs} (on the left) and GIT PEM simulating space-like environment demonstrating that ground testing under-estimates the life metrics, V_{ebs} (on the right)



C. Electrospray Plume Divergence

Electric propulsion systems require careful consideration of plume divergence and evolution over a range of operating conditions and environments. Existing means of describing plume divergence such as outlines, plume profiles, and snap shots of the plume are dominated by outlier particles and do not provide reliable or quantitative insight due to species dependence. Small, mobile particles are rapidly pushed away from the dense plume center and exit the interaction region earlier than larger species, which remain confined near the axis. This segregation shows that there is no single radial threshold for all particles, but rather one that depends on both species and position. Importantly, some large, on-axis particles remain within the interaction region far downstream due to sustained Coulomb interactions, meaning their behavior cannot be simplified by assuming interactions end at a fixed threshold. This insight highlights that plume modeling must remain species- and position-specific to capture realistic particle behavior.

A second focus is plume divergence, a property that directly impacts thruster lifetime and performance but lacks a standard definition in the electrospray community. Traditional measures, like outlining extreme trajectories, exaggerate divergence, while snapshots are not quantifiable. Equation (3) provides the classical definition of beam divergence—radial expansion over distance—but electrosprays have no sharp boundary to apply it directly.

$$\theta = \arctan\left(\frac{\Delta r_{b}}{l}\right) \tag{3}$$

$$\theta_{3\sigma} = \arctan\left(\frac{\Delta r_{3\sigma}}{z}\right) \tag{4}$$

To resolve this, we define the plume edge statistically using three standard deviations (3σ) of a Gaussian fit to particle density. Substituting this 3σ boundary into Eq. (3) yields a divergence measure that captures the bulk of the plume while excluding outliers, offering the first consistent, quantitative way to compare plume divergence across systems. Complementing this, the use of emittance (Eq. 5) brings in a beam-physics metric that tracks how particle momentum spreads with position, revealing that divergence grows downstream due to Coulomb scattering but should plateau beyond strong interaction regions.

$$x = \frac{1}{\pi} \int \int dx dx' \tag{5}$$

where the angle is the ratio of momentum in a transverse direction to momentum in the axial direction,

$$x' = \frac{p_x}{p_z} \tag{6}$$

Finally, at the emission site, molecular dynamics simulations show that nanoscale droplet breakup under high electric fields governs initial ion extraction, with mobility differences among ions shaping early plume structure. Together, these models and equations establish a framework that links nanoscale emission physics to plume-scale divergence, directly tying fundamental physics to thruster performance⁶.



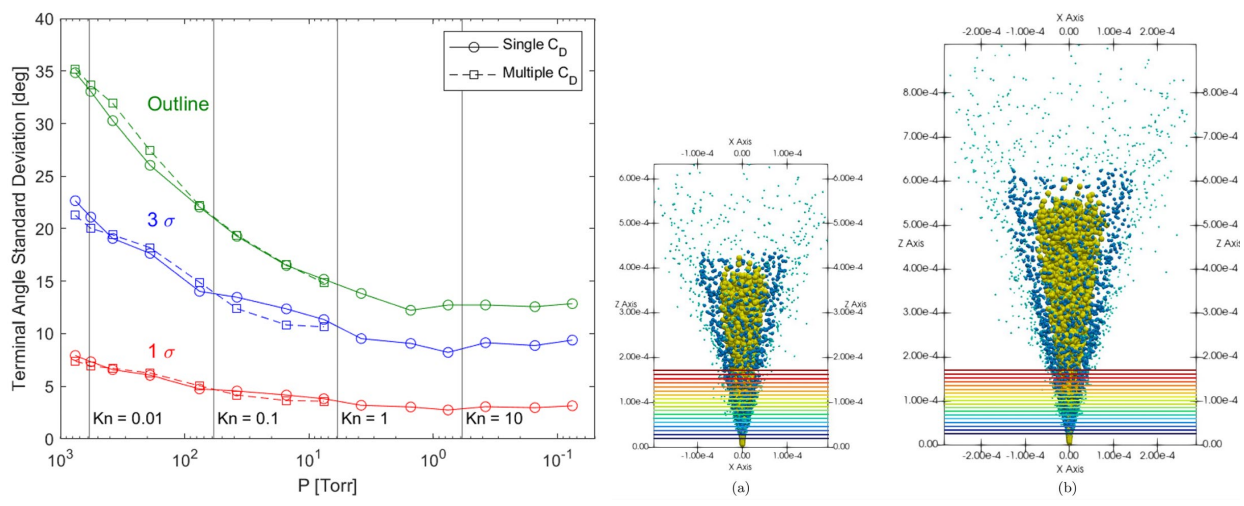
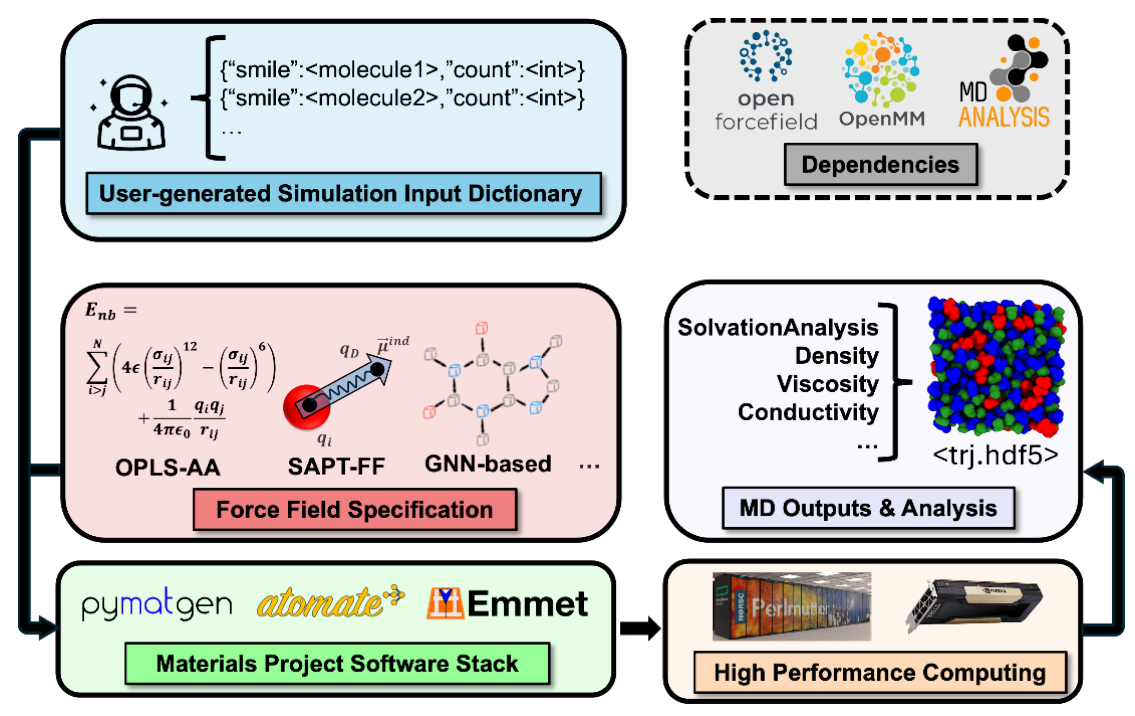


Figure 5: Left: Terminal angle measurements at the collector plate location are given for 1 and 3 standard deviations of particle number density and the outline of plumes simulated at different background pressures. Right: Cross sections of the tri-species EMI-Im plume used to observe emittance evolution.

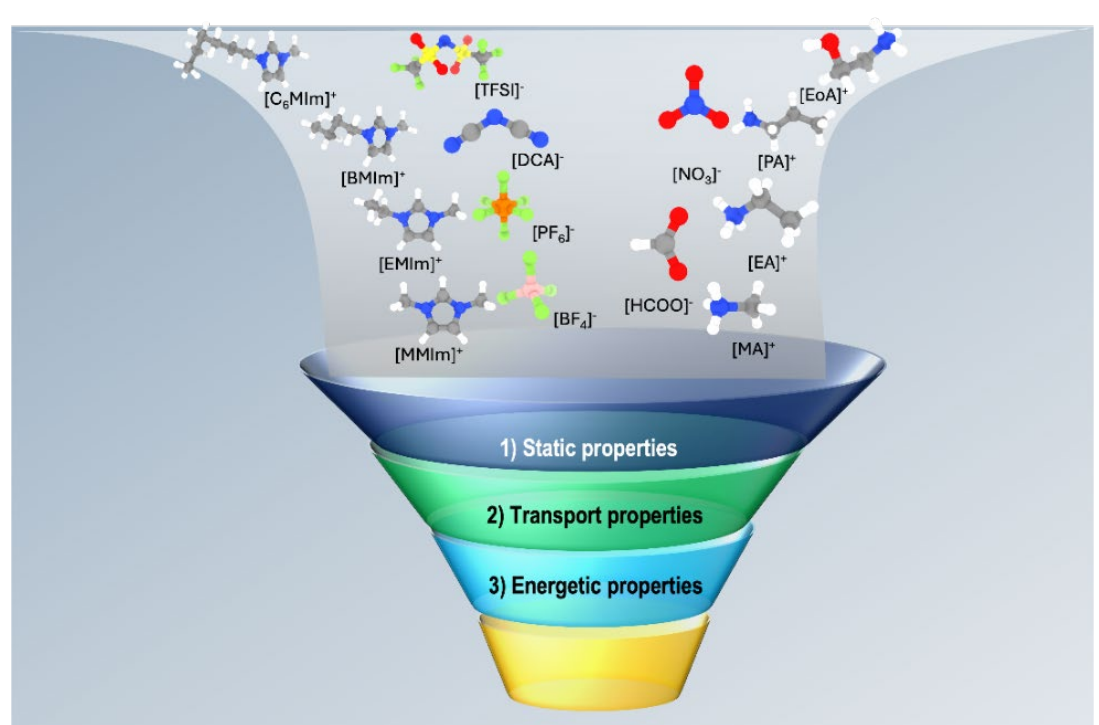
D. Multimode Propulsion Propellant Research

Multimode propulsion (MMP) technologies combine chemical and electric propulsion systems across shared thruster hardware, resulting in promising dry mass savings, space mission flexibility, and cost benefits^{7,8} MMP performance is directly linked to liquid propellant properties: on one hand, chemical propellant performance depends on chemical potential energy, while electric propellant performance on static, electrical, and transport properties⁹. Naturally, the task of propellant selection is met with the challenge of an expansive chemical design space at the intersection of (sometimes competing) chemical functions. Our recent research efforts have focused on understanding ionic liquid (IL) MMP propellants¹⁰⁻¹², a class of room temperature, organic salts composed of tunable^{13,14} cationanion pairs with desirable thermophysical properties (e.g., low vapor pressures, high ionic conductivities, low toxicity). In order to expedite maturation of MMP technologies, we have developed a computational, high-throughput screening paradigm built upon the Materials Project¹⁵ software ecosystem to conduct virtual screening of MMP propellant "hits", or ILs that optimize chemical and electric propulsion requirements. As shown in Fig. 6a, the highthroughput framework is a user-driven pipeline built upon the Materials Project (MP) software stack (i.e., atomate2¹⁶, pymatgen¹⁷, Jobflow¹⁸, FireWorks¹⁹), enabled by the accurate, ab initio-based molecular dynamics (MD) force fields (e.g., OPLS-AA²⁰, SAPT-FF²¹, graph neural network-based force fields²²), and powered by modern high performance computing (HPC) resources. Figure 6b depicts a conceptual screening funnel, in which candidate IL propellants are systematically down selected through tiers of computationally accessible properties. At the top-most tier, equilibrium MD simulations provide static properties like liquid density, enthalpy of vaporization, and short- and long-range structural properties. Contingent on sufficiently converged statistics, transport properties (e.g., viscosity, conductivity, self-diffusion coefficients) are also accessible via equilibrium MD. Energetic properties remain an area for future work. In summary, this hierarchical approach enables rapid identification of "hits" that satisfy MMP performance criteria while reducing the time and computational expense typically associated with brute-force exploration of the IL chemical space.





(a) Overarching computational high-throughput screening framework.



(b) Screening workflow with hierarchical approach to computing thermophysical properties via molecular dynamics.

Figure 6: (a) High-throughput molecular dynamics (HTMD) pipeline framework. (b) Hierarchical screening funnel for computing thermophysical properties.



III. EP Plasma Physics

A. Global Plasma Modeling

Improved insights into RF plasma processes are vital to understanding and harnessing inductively coupled plasmas for propulsion applications with both noble and molecular propellants. This motivates the development of spatiotemporal diagnostics to resolve the plasma behavior in space and time, for instance FastOES which aims to discriminate dynamics occurring over time periods towards that of the driving RF oscillation. To support such diagnostics, an area of study is the development of a modeling framework, which is deliberately low-cost and intended as a reference to more sophisticated multi-physics models that can be pursued in future. In this case, the modeling approach combines: A global plasma model (GPM), to predict the plasma parameters for given inputs and a collisional radiative model (CRM), to predict the optical emission spectrum for given plasma parameters.

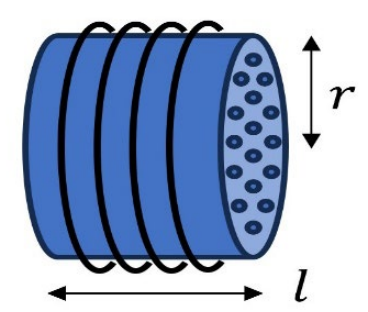


Figure 7: Simplified geometry assumed in GPM, showing RF helical coil antenna and extraction grids (right).

The GPM considers a spatially averaged plasma, i.e. a single-cell domain, for a cylindrical plasma chamber with an external RF coil antenna and including extraction grids, as shown in Fig 7. As a first step, both the GPM and CRM are developed for xenon gas and assume a Maxwellian electron energy distribution function. The GPM integrates four key equations, representing the particle and power balance in the plasma, for four primary variables: neutral gas density (ng), electron/ion density $(n_e \approx n_i)$, neutral gas temperature (T_g) , and electron temperature (T_e) . The GPM is based on that of Chabert et al.²³, including rate equations formulated as:

$$\frac{dn_g}{dt} = \frac{Q_{in}}{V} + n_e u_B \frac{A_{i,2}}{V} - n_e n_g K_{iz} - \Gamma_g \frac{A_g}{V}$$
(7)

$$\frac{dn_i}{dt} = n_e n_g K_{iz} - n_i u_B \frac{A_{i,1}}{V} \tag{8}$$

$$\frac{d}{dt}\left(\frac{3}{2}n_gk_BT_g\right) = 3\frac{m_e}{M}k_B\left(T_e - T_g\right)n_en_gK_{el} + \frac{1}{4}Mu_B^2n_en_gK_{in} - \kappa\left(\frac{T_g - T_w}{\Lambda_0}\right)\frac{A}{V}$$
(9)

$$\frac{d}{dt}\left(\frac{3}{2}n_e k_B T_e\right) = P_{abs} - P_{loss} \tag{10}$$

Here, Equations 7 and 8 represent the neutral and ion particle balance, respectively, while Equation 9 represents the neutral power balance. Equation 10 represents the power balance of the plasma electrons, which includes the RF power absorbed solely by the electron population (P_{abs}) and the energy lost by electrons to support various plasma processes (P_{loss}) . These are defined as:



$$P_{abs} = \frac{1}{2} \left[R_{ind} + (\omega^2 L_{ind} C)^2 R_{cap} \right] I_{coil}^2$$
 (11)

$$P_{loss} = \varepsilon_{iz} n_e n_g K_{iz} + \varepsilon_{ex} n_e n_g K_{ex} + \frac{3m_e}{M} k_B (T_e - T_g) n_e n_g K_{el} + 7k_B T_e n_e u_B \frac{A_{i,1}}{V}$$
(12)

Equation 11 expresses the absorbed RF power as a function of the effective electrical circuit parameters of the plasma, which in turn can be defined in terms of the neutral and electron densities and temperatures. This approach is based on a transformer analogy, whereby the RF coil forms the driving circuit and the plasma electron current acts as a single driven winding²⁴.

The CRM models the number density of 36 excited states of neutral xenon (Xe I), as well as the ground and ion states. Such an approach aims to sufficiently and accurately capture the population of the ten 6p/6p' (2p1-10 in Paschen notation) states and the four 6s/6s' (1s2-1s5) near-ground states, which form the upper and lower states respectively of the radiative decays that dominate the plasma optical emission spectrum in the 800-1000 nm wavelength range. The population of each state p is expressed as a function of excitations/de-excitations from all the other considered states q, including both collisional and radiative terms as shown in Equation 7. The predicted intensity of light emission at each radiative transition wavelength is adjusted for photon absorption by the plasma²⁵.

$$\frac{dn_p}{dt} = \sum_{q} n_e K_{qp} n_q - \sum_{q} n_e K_{pq} n_p + n_i K_{ip} n_0 + \sum_{q} n_q A_{qp} - \sum_{q} n_p A_{pq}$$
(13)

The GPM and CRM are compared to experimental data of a 3 cm diameter RF-ionization gridded ion thruster operating on xenon²⁶, which includes both thruster performance (beam current with input RF power) and time-averaged OES measurements. The thruster operation on xenon is shown in Figure 8, whereby the OES lens was positioned to observe the internal thruster plasma through the quartz discharge chamber. Figure 8 also presents a comparison of the beam current as a function of the RF power between the GPM and experimental thruster. While the GPM successfully captures the shape and trend of the experimental curves, it suggests that a beam flatness correction of around 80 % should be applied to the GPM values, accounting for the radial non-uniformity of the ion density that occurs upstream of the ion thruster grids due to the presence of the discharge chamber walls.



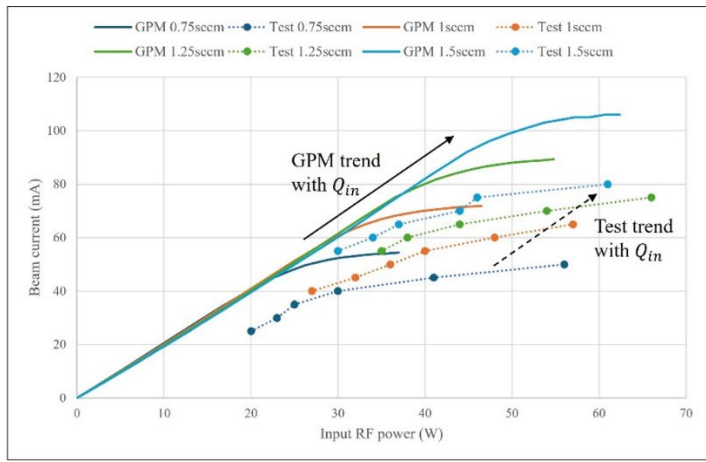


Figure 8: 3cm diameter RF gridded ion thruster operating on 0.75-1.5 sccm Xe and 20-60 W input RF power [4]. Beam current vs RF input power comparison between GPM prediction and experimental data, for varying xenon flow rates (Q_{in}) .



The CRM-predicted spectra are compared to the experimental OES data for eight major emission lines from 823 nm to 916 nm, evaluating the CRM over a range of electron density and temperature values and using a least squares error approach to minimize the error in normalized peak intensity to the experimental data. The results are shown for two thruster flow rates in Fig.9, indicating an average electron temperature of 2-2.5 eV and ionization fraction around 0.2 % in the internal thruster plasma. To first order, an increase in the xenon flow rate results in a fall in T_e and rise in n_e , as expected given an increased plasma collisionality.

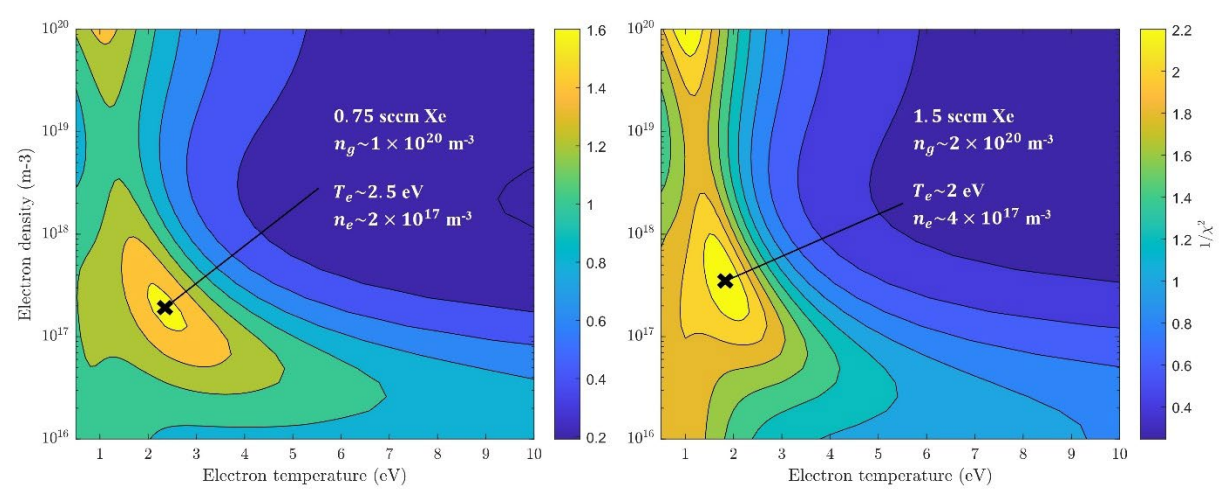


Figure 9: Inverse of least squares error $(1/\chi^2)$ between CRM and OES data for thruster operation at 0.75 sccm Xe (left) and 1.5 sccm Xe (right), as a function of electron density and temperature. CRM-predicted T_e and n_e are labeled.

Future work on the GPM and CRM development will focus on: i) a study of GPM-CRM agreement in plasma properties over the thruster operating envelope, ii) an assessment of the key model sensitivities to uncertain inputs, and iii) an analysis of the time-resolved plasma behavior and electron energy loss pathways modelled by the GPM.

B. FastOES

Fast Optical Emission Spectroscopy (FastOES) is a non-intrusive method for taking temporally resolved measurements of electron temperature and density. Standard OES techniques using spectrometers require relatively long integration times to detect low-light signals, limiting it to time-averaged measurements which mask transient plasma dynamics. FastOES is capable of temporally resolving oscillatory behavior by prefiltering the optical signal for two specific wavelengths of interest, then measuring each with high-speed, high-gain photomultiplier tubes. The low-cost, non-intrusive, and passive nature of these measurements allows us to extend diagnostic capabilities to new plasma regimes and higher density plasmas. FastOES was initially employed on a xenon Hall thruster to observe the breathing mode, a well-documented low frequency oscillation between 10-50 kHz²⁷.

Recent work has advanced the application of FastOES for resolving plasma instabilities in Hall thrusters²⁸: applied to a krypton-fed 9 kW-class Hall thruster, FastOES provided temporally resolved measurements of both the anode discharge channel and the centrally mounted hollow cathode plasma plumes¹⁰. Simultaneous FastOES and current measurements revealed global low-frequency oscillations (4–5 kHz), anode-focused breathing-mode oscillations in the 10–25 kHz range, and a broad 30–55 kHz band localized to the cathode. A sharp, highly coherent 130 kHz feature was observed in cathode-focused FastOES, weakly present in current measurements and absent in the anode channel, suggesting a cathode-localized origin. Continuous wavelet analysis showed these oscillations occur in bursts modulated at lower-frequency bands, indicating potential coupling between different cathode instabilities. These higher frequency oscillations demonstrated weak coupling back to the thruster's electrical circuit and did not appear in anode measurements, further proving the capability of FastOES to non-intrusively measure plasma born instabilities only previously measured using perturbing diagnostics. FastOES distinguished broadband and narrowband



oscillations with higher fidelity than conventional current measuring diagnostics, providing insight into plume dynamics and cathode-anode coupling mechanisms.

Complementary efforts in the lab have focused on extending optical diagnostics to other plasma regimes. Simplified radiofrequency (RF) plasma sources also in development by the group have been used in this work to help identify candidate emission lines for FastOES in alternative propellants. Together, these efforts broaden the applicability of FastOES beyond Hall thrusters and support the development of predictive models for facility effects and cathode life-limiting processes.

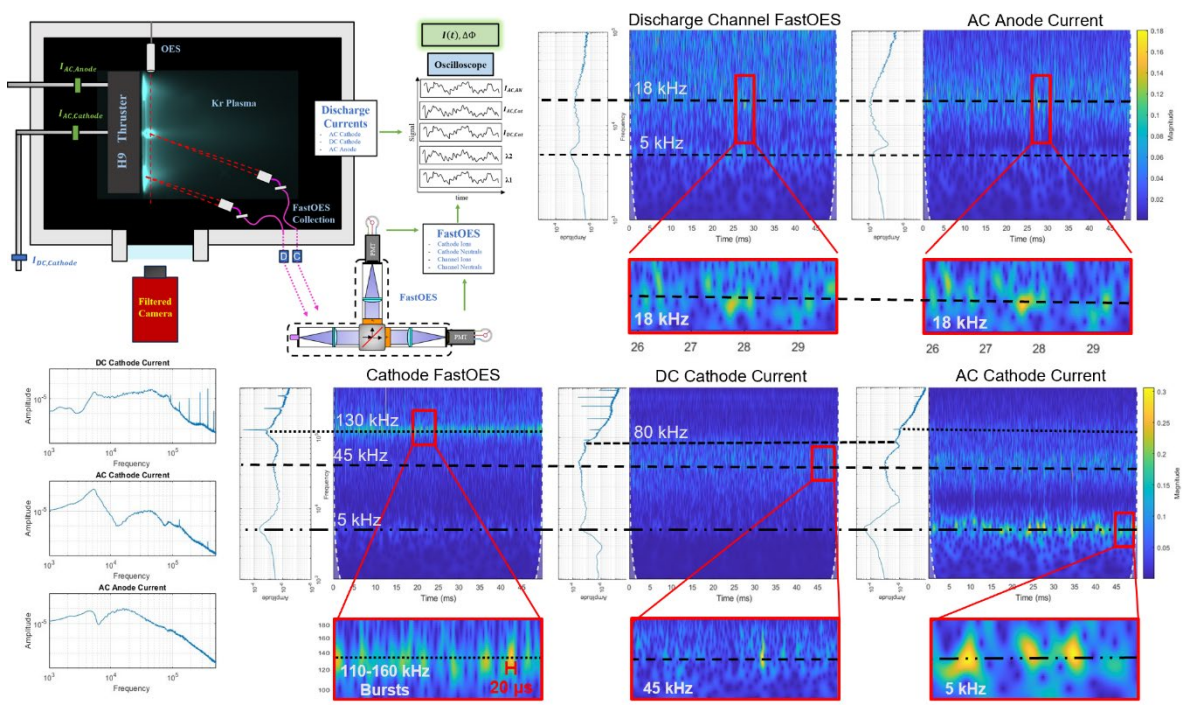


Figure 10. Diagram of Hall thruster experiment (top left) and a summary of results showing continuous wavelet transforms and power spectral density plots of optical and electrical signals with key frequencies highlighted.

C. Spatial OES

In 2024, we began exploring spectral imaging as an application of spectroscopy for Hall thrusters with both xenon and krypton²⁹. Building on that work, we have continued these efforts on a different Hall thruster with an internal cathode configuration to extend our analysis³⁰. Using a monochrome low-light camera equipped with different narrow bandpass filters, we performed spatial spectroscopy on a krypton-fed thruster to investigate how cathode configuration influences the distribution of ion and neutral species in the plume. The filtered images were scaled to absolute intensity using standard Optical Emission Spectroscopy (OES) measurements, enabling both qualitative and quantitative interpretation. We applied tomographic techniques, including inverse Abel transforms, to reconstruct radial intensity profiles of the plasma and estimate relative beam current with respect to position based on plume brightness. By aligning and comparing images across ion and neutral wavelengths, we generated emission ratio heatmaps that depict regions of increased ionization. These methods not only provide spatially resolved insights into species transport in Hall thruster plumes, but also lay the groundwork for future work with collisional radiative models to produce spatial maps of electron temperature or density during thruster operation.



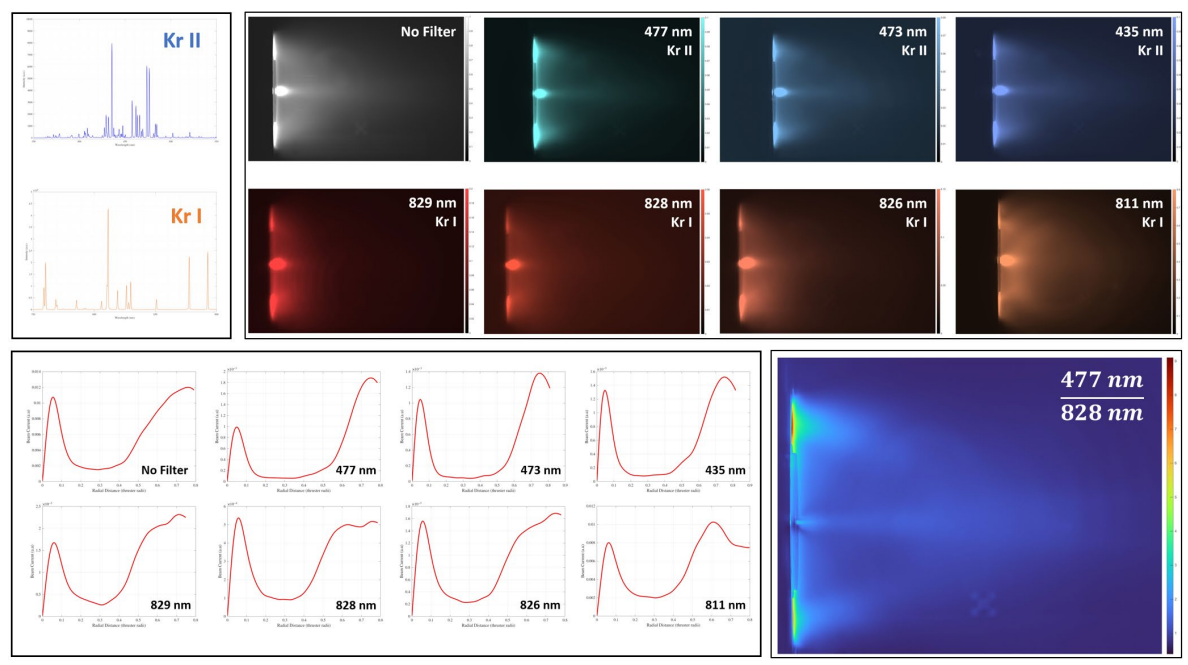


Figure 11. Top Left: OES spectra collected during a test of the H9 thruster on krypton, split between typical ranges for Kr II singly charged ions and Kr I neutrals. Top Right: filtered images of Kr II (top row) and Kr I (bottom row) from a thruster plume, using a total of 7 filters. Bottom left: Reconstructed measurements of relative beam currents retrieved from brightness measurements near the thruster exit plane. Bottom right: Heatmap of relatively high Kr II emission (red) and Kr I emission (blue) throughout the thruster plume.

D. PESPL Radiofrequency Tests

RF gridded ion thrusters are promising for ABEP because they avoid oxygen-sensitive hollow cathodes and are simpler and more robust than DC or microwave thrusters, enabling rapid lab testing. Previously, one such thruster was developed within the lab to explore air-breathing performance²⁶. Expanding on that work and demonstrating the versatility of the design, an RF cathode has now also been built using similar geometry (Fig 12). The development of the cathode was not without setbacks as the geometry of the original design resulted in excessive electron losses to the walls, thus hampering ignition. Decreasing the ratio of surface area to volume, the newly developed RF cathode was capable of outputting up to 80 mA of current on approximately 20 W input power defined as the difference between forward power and reflected power. Initial tests were conducted prior to achieving an optimal match with the matching network.

Underscoring the promising nature of RF plasma discharges, OSU has developed a canonical rf experiment. This experiment has been nicknamed the "Phantom Tube," and is used to study power coupling, electron and ion dynamics that govern discharge performance. The Phantom Tube is a 2" diameter by ~6" long quartz glass flange that mounts to the side of a 24" diameter by 36" long vacuum chamber. Filling the chamber with gas, we ignite the plasma with a helical RF antenna mounted around Phantom tube. The antenna and all electronics are easily accessible outside the vacuum chamber, allowing for rapid iterations in the study of antenna design, match network configurations, and non-intrusive diagnostic access.

Enabling the rf gridded ion thruster, cathode and Phantom tube is the electrical model informing our match network design. Optimal power coupling is achieved when the source impedance and load impedance are equal. A standard source impedance is usually 50 Ω , however 75 Ω sources exist as well. At Oregon State, all of our RF equipment is rated to 50 Ω . Typically, RF loads are designed precisely to match the source, however plasmas are a dynamical system and thus it is difficult to predict its impedance prior to testing. This is why it is critical to develop a reasonable model of the electronics, inputting an educated guess for the plasma impedance, in order to operate and rf plasma safely and efficiently.



Building on the work of Chen³² and Piejak³³, we developed an L-type match network consisting of only a series and shunt capacitors (Fig. 12). By constraining the design to capacitors, we are able to close the impedance calculations and derive an analytical model of the electronics. Additionally, experience taught us that inductors may couple to surrounding conductive surfaces normal to the axis of the inductor, thus providing a pathway for parasitic power loss which we aim to avoid. Equations 3 and 4 calculate the series and shunt capacitors respectively. In the match network calculation, $Z_{net} = R + jX = Z_{coil} + Z_{plasma}$ and ω is the rf driving frequency. For simplicity, we have defined an effective impedance, \hat{X} (Equation 5) which we take as its value only the positive solution to Equation 6 in order to ensure C_{shunt} and C_{series} are positive. Otherwise, a negative capacitance would imply the need for an inductor in place of the capacitor.

$$C_{series} = \frac{R^2 + \hat{X}^2}{\omega \hat{X} (R^2 + (\omega L)^2)}$$
(3)

$$C_{shunt} = \frac{\omega L - \hat{X}}{\omega (R^2 + (\omega L)^2)}$$
 (4)

$$\hat{X} = \sqrt{\frac{R^3 + R(\omega L)^2}{R_0} - R^2}$$
 (5)

Understanding the plasma impedance is critical to iteratively designing the match network and can provide insights into the power deposition and plasma parameters of the load discharge [Chabert].

$$Z_{plasma} = \frac{Z_{shunt}(Z_{net} - Z_{series})}{Z_{shunt} - Z_{net} + Z_{series}} - Z_{coil}$$
(6)

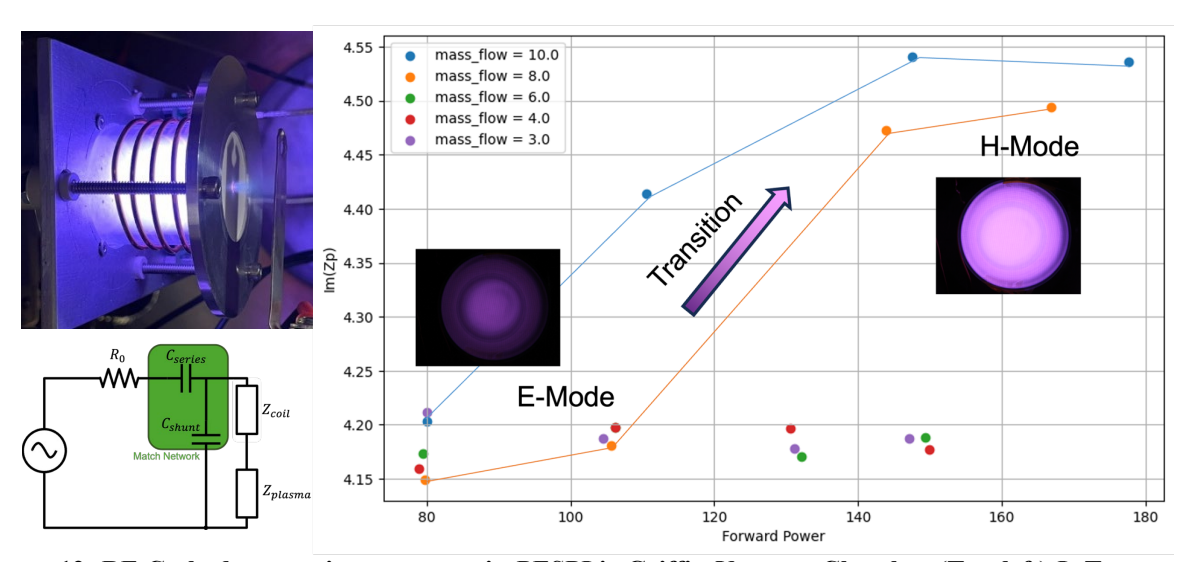


Figure 12. RF Cathode operating on xenon in PESPL's Griffin Vacuum Chamber (Top left) L-Type match network used for all RF efforts in PESPL (Bottom Left) Measuring the plasma inductance as a function input power demonstrates the transition from E to H model and illustrates the transition's dependence on plasma density (Right)



IV. Plasma Material Interactions

A. Sputtering Models

To inform our predictions of sputterant behavior and plan experimental observations during hall thruster operation within a facility, we investigated the behavior of propellant-related sputtering yields for various chamber surface materials³⁴. The ion-irradiation Monte Carlo program, TRI3DYN, simulates carbon sputtering, reflective scattering, and post-implantation ejection of xenon from test chamber materials. Outputs of the carbon sputtering yield show good alignment with published data after parameterizing the TRI3DYN code with physically-grounded adjustments of the surface binding energy scaling (SBES) and maximum atomic ratio of xenon-in-carbon implantation (EXST, EXcess Stoichiometry Treatment) parameters. The binary collision approximation has historically been unreliable at "low" energies due to missing physics. However, an analysis of reduced energies toward the validity of the BCA suggests that the ion-solid-energy system of interest can show realistic results for xenon-carbon-300eV interactions³⁵. To properly model the trajectories and energies of emissions from chamber walls, research into the bonding environment of plume-exposed materials is necessary given that the scatter angle and resulting energy are functions of these energy loss terms.

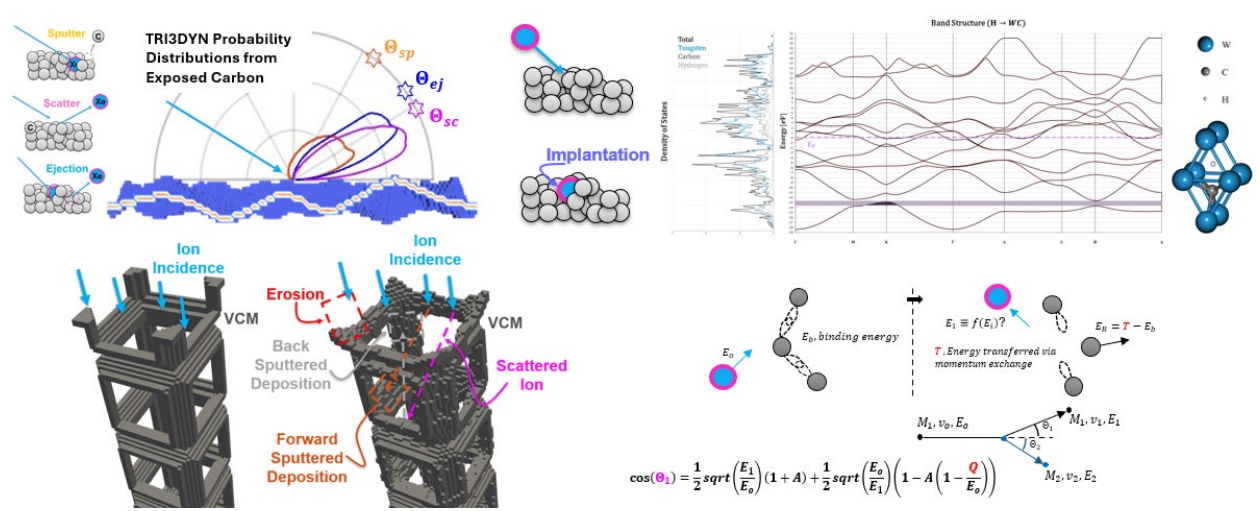


Figure 13. Detailed modeling of sputtering behavior for chamber surfaces. In these models, we track scattering, implantation, and sputtering and ejection of implanted particles. On the left, scattered, sputtered, and ejected particle PDFs are simulated from a roughened carbon surface. These initially flat-plane simulations can be augmented for simulating volumetrically complex materials, informing us of local sites of growth and erosion from the ion-solid interactions. On the right, an ab-initio calculation of hydrogen-impregnated tungsten carbide reveals differences from WC's pure band structure even without bonding from the impregnated species. This principle is crucial in understanding energy losses during the collision calculations of the chamber material's BCA simulation, shown schematically in the bottom right.

B. Carbon Material Investigations

Electric propulsion ground testing is limited in predicting thruster lifetime analysis due to multiple facility effects such as carbon sputtering, erosion, and deposition across the inner surfaces of both the thruster and vacuum chamber facilities. While known fuel sources, argon and xenon have been tested in numerous studies, the sputtering yield and erosion due to krypton requires additional analysis³⁷. In collaboration with JANUS, PESPL participated in a Facility Interpolation test³⁶ to investigate the inner walls of the chamber and beam target after several ignition tests using NASA's H9 thruster. Images of the macroscopic geometry of Georgia Institute of Technology's graphite beam target were taken to compare against previous computational and experimental data regarding the ending steady state surface morphology for better sputter yield predictions. Looking at the surface characteristics of the beam target's center, the surface morphology appears to have random macroscopic characteristics that are not consistent with more traditional



surface flattening features exhibited from carbon-carbon materials^{38,39}. Current experimental results from this experiment show that steady-state surface morphology does not evolve to a regular or flat surface due to long-term irradiation but maintains macroscale features that should be considered for sputtering behavior predictions that account for geometric trapping at sputtered surfaces⁴⁰.

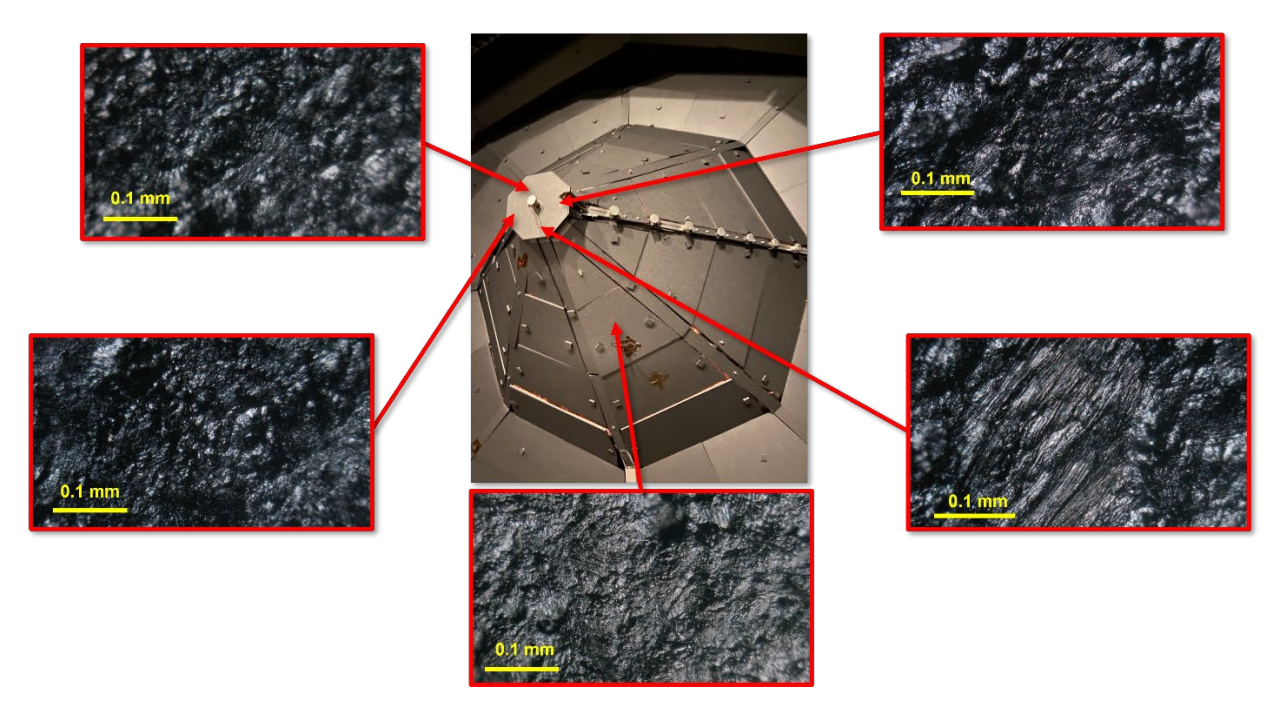


Figure 14. Georgia Institute of Technology's Beam Target inside of VTF-2 after hundreds of hours of exposure using various propellants for both commercial and research thruster testing operations⁴⁰.

Future work will include material analysis of the crystallographic variations between typical carbon materials used in EP test facilities to investigate why surface topological features are different between species. Comparisons will be made using similar ion-bombardment test conditions as function of angular dependence to highlight uncertainty in available literature that this further addressed in section IV.C.

C. Literature Comparisons

In support of testing efforts, a review of carbon sputtering for vacuum facility materials is presented showcasing yields versus different propellants. As shown in the figure below, multiple studies have been used with different forms of carbon such as pyrolytic graphite (PG), carbon-carbon composites (CC), and high-density graphite (HD). Combined with the results of the recent FIT experiment, this data collection suggests that the crystal structure and surface topology of the material may play significant roles in the material's sputter yield mitigating criterion⁴⁰. Further investigations of their influence are ongoing with HPESPL's efforts. Regardless, the general trend shows that krypton should produce the least number of sputtering particles when comparing against argon and xenon at normal incidence.



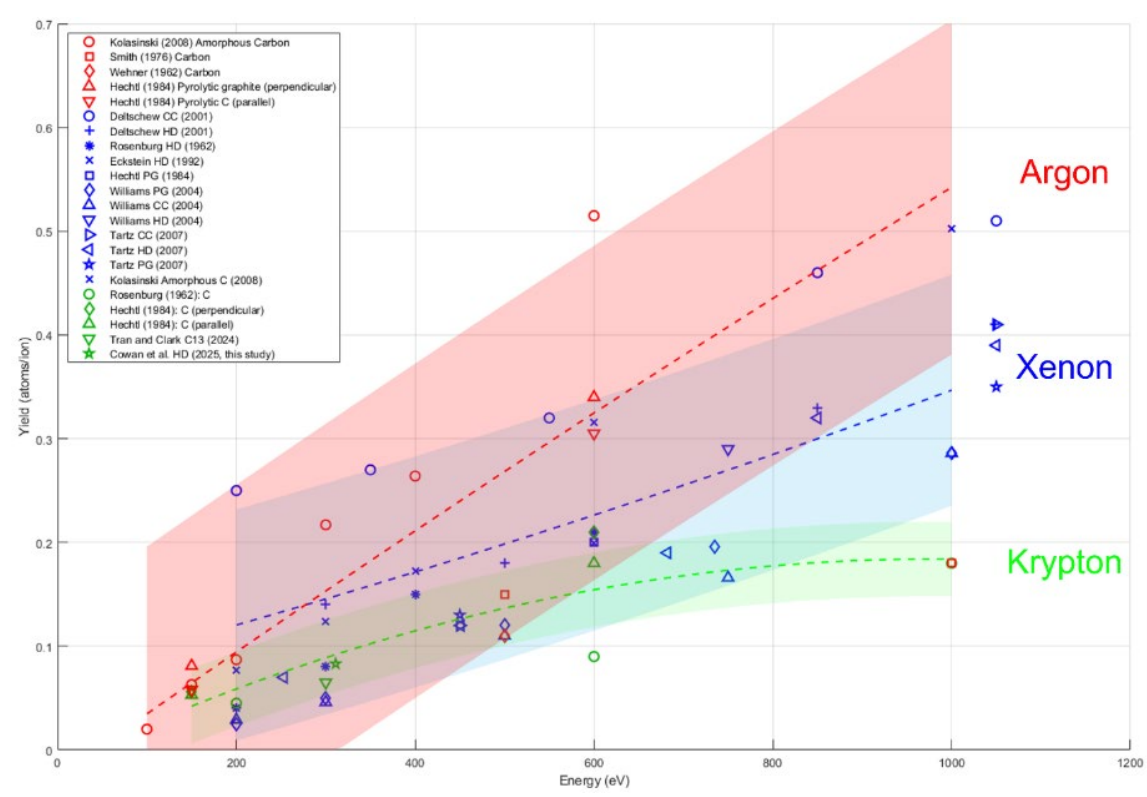


Figure 15. Sputter yields of carbon materials at normal incidence varying with ion energy⁴⁰, featuring citations⁴¹⁻⁴⁷

D. Volumetrically Complex Materials

Volumetrically complex materials (VCMs), such as stochastic foams and grid-like structures, offer a promising solution to the erosion-driven limits of featured surfaces by reducing sputtering yields by up to 80% through geometric trapping^{49,50}. Their performance is described by the plasma infusion parameter, ξ , defined as the ratio of mean pore diameter to local sheath length, $\xi = \frac{D}{L_s}$, which maps plasma—material interactions across regimes ranging from plasma-facing to plasma-infused⁵¹. This framework highlights how VCM structure and applied bias influence transport: while open-cell designs promote plasma infusion, negatively biased VCMs generate expanded ion sheaths that shift transport toward ballistic ion trajectories. Canonical experiments and analytical models are being used to capture this transition and refine understanding of plasma transport in complex geometries⁵¹.

Additive manufacturing (AM) enables the fabrication of VCMs with tailored structures that enhance current capacity and erosion resistance, while also serving as testbeds for sputter transport studies⁵¹. Although AM introduces imperfections like spatter or unmelted regions, erosion often removes these artifacts and may even expose voids that contribute to sputterant trapping—suggesting design opportunities. In parallel, particle-tracking Monte Carlo simulations informed by binary-collision data are being applied to electric propulsion test facilities⁵². These models show that VCMs not only mitigate sputterant deposition on sensitive surfaces but also provide actionable pathways for chamber optimization. Collectively, these advances demonstrate that VCMs, guided by the infusion parameter ξ , offer a durable and tunable approach for controlling plasma—material interactions in electric propulsion systems^{51,52}.



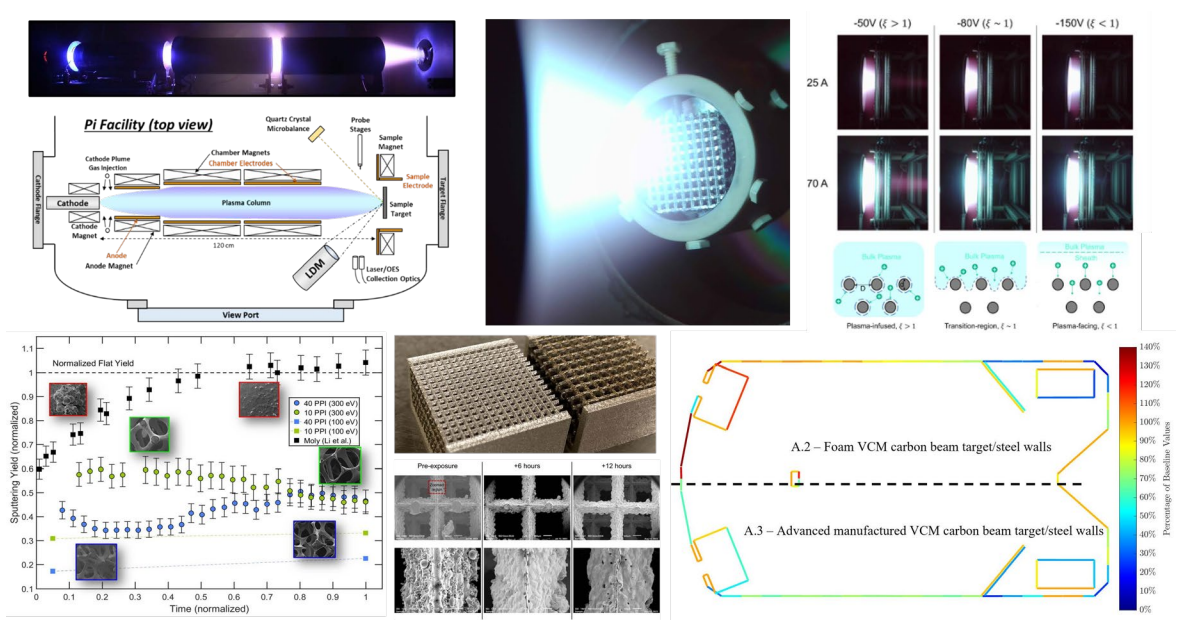


Figure 16. Summarizing PMI efforts. We have developed volumetrically complex materials the yield significant and persistent sputter reduction for EP applications. During this effort, we discovered and characterized the regime of plasma-infusion as the ratio effective pore size to sheath length. These efforts have led to computationally informed VCM optimization that can yield significant reductions to facility backsputter to the thruster.

E. Ion-Induced Electron Emission

Ion-induced electron emission (IIEE) from facility walls during testing is one of the largest sources of uncertainty and should be properly quantified. IIEE is usually described by γ , which represents the number of electrons ejected per incoming ion. There are two main mechanisms by which an electron can be excited above vacuum level by an impinging ion: **a)** If the electron is emitted after neutralization of the incoming ion at a finite distance from the surface, this process is widely known as potential electron emission (PEE) or Auger emission. **b)** If the electron is emitted because of the slowing of the ion once the surface is penetrated, or in other words, because of kinetic energy loss, the process is known as kinetic electron emission (KEE). We have developed models that describe and quantify both KEE⁵² and PEE⁵³ in the energy regime correspondent to ion velocity measurements at the sheath for Ar, Kr, and Xe projectiles, but which should be valid for other projectile species as well.

Our approach to model PEE was to assume Auger neutralization (AN) by restricting the resonant neutralization channel for projectiles where the local work function at the surface was larger than the lowest-lying excited state of the incoming ion measured with respect to the vacuum $\Phi > E^*$, where Φ is the local work function, and E^* the excited level of the ion. By merging this approach with a Fermi – Dirac distribution of electrons at the surface, we were able to reproduce experimental work by solely fitting the distance of neutralization from the surface to account for electronic level shifts. Furthermore, we provided yields and emitted electron distributions for 45+ unexplored ion-target combinations. We strongly encourage anyone interested to read the referenced paper as it is theoretically dense and contains a thorough description of PEE.

On the other hand, KEE is much more complicated to model, especially at low energies and for heavy ions such as those utilized as propellant for EP applications. Furthermore, developing a general theory that describes KEE is challenging since this process is heavily dependent on the microstructure at the surface, impact geometry, composition, ion species, fluence, amorphization, or velocity regime to name a few. At ion velocities larger than roughly 10^7 cm/s, a binary collision model between the projectile and target conduction electrons described by Fermi-Dirac statistics usually yields a decent approximation, where the yields increase linearly with velocity. This was our first approach to KEE⁵². However, at lower energies this approach is invalid because of the size mismatch between the projectile and



electrons, where the energy gain is constrained by momentum conservation $E_{max} = 2mv (v + v_e)$, where v = projectile velocity, m = mass of an electron, and $v_e =$ velocity of a conduction electron given by Fermi statistics.

At present, we are developing a multi-physics model that builds upon our previous work^{1,2} to provide precise IIEE results encompassing both PEE, and KEE without the need for fitting parameters and a reduced set of assumptions. Inputs to our new model are: ion-target species, impact energy, ionization state, and angle of approach. The idea is to utilize TRIM to track the trajectory of the main projectile and recoils, then to properly account for electronic excitations, and finally to track the trajectory of electrons until thermalization or escape with the use of an in-house raytracing model^{53,54}. Figure 17 shows a schematic of our model with the main physical mechanisms that we believe are important for emission in the low-to-medium kinetic energy regime.

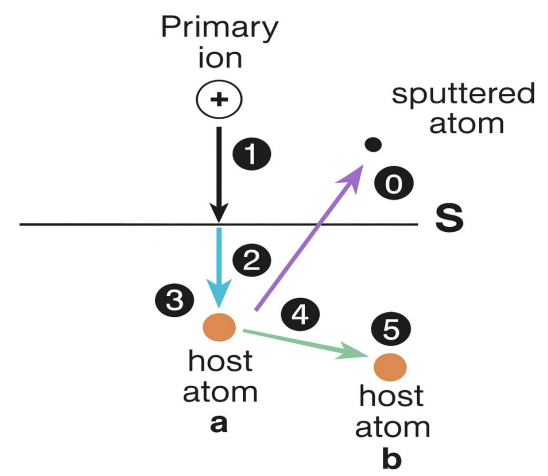


Figure 17. Schematic of our new model (work in progress) for IIEE in the low-to-intermediate energy regime showing the different physical processes that are most relevant to electron excitation and emission. Here: 0) Electron emission from sputtered atoms by inner-shell ionization and Auger decay in vacuum. 1) Potential electron emission by Auger neutralization. 2) Emission of s-band conduction electrons by quasi-free binary collisions with main projectile. 3) Emission of d-band or outer p-band electrons after electron excitation by electronic friction from the interaction of the projectile and host atoms. 4) Same as (2) but for recoils. 5) Same as (3) but for recoil-host interactions.

F. Cold Atmospheric Plasmas

Over the past two decades, cold atmospheric plasmas (CAP) have become a key area of research and application. CAP devices generate partially ionized plasmas at atmospheric pressures and temperatures, suitable for diverse applications⁵⁵, including material processing and medical uses like sterilization and treatment of hard-to-reach skull base tumors⁵⁶. During the COVID-19 pandemic (2020-2022), PESPL and UCLA collaborations demonstrated that CAP effectively inactivates the SARS-CoV-2 virus, reducing transmission^{57,58}.

At PESPL, we focus on two main aspects of CAP: plasma infusion of volumetrically complex materials (VCMs) and controlled generation of reactive species. For conductive VCMs like metal foams, maintaining appropriate porosity (average pore size larger than twice the Debye length) extends the plasma discharge region into the material, enhancing reactive species generation, similar to traditional plasma systems⁵⁸. This process is influenced by air composition, humidity, and device parameters, and we are optimizing these for targeted species generation in various environments. Applications include wound healing and tumor treatment, both directly and indirectly⁵⁹⁻⁶¹. CAP also shows promise in material processing by modifying surface properties and enhancing adhesion for industrial applications⁶². Recent studies highlight aluminum foam's role in clinical plasma applications, effectively filtering sparks and delivering reactive species, thus improving CAP efficacy in biomedical settings⁶³.



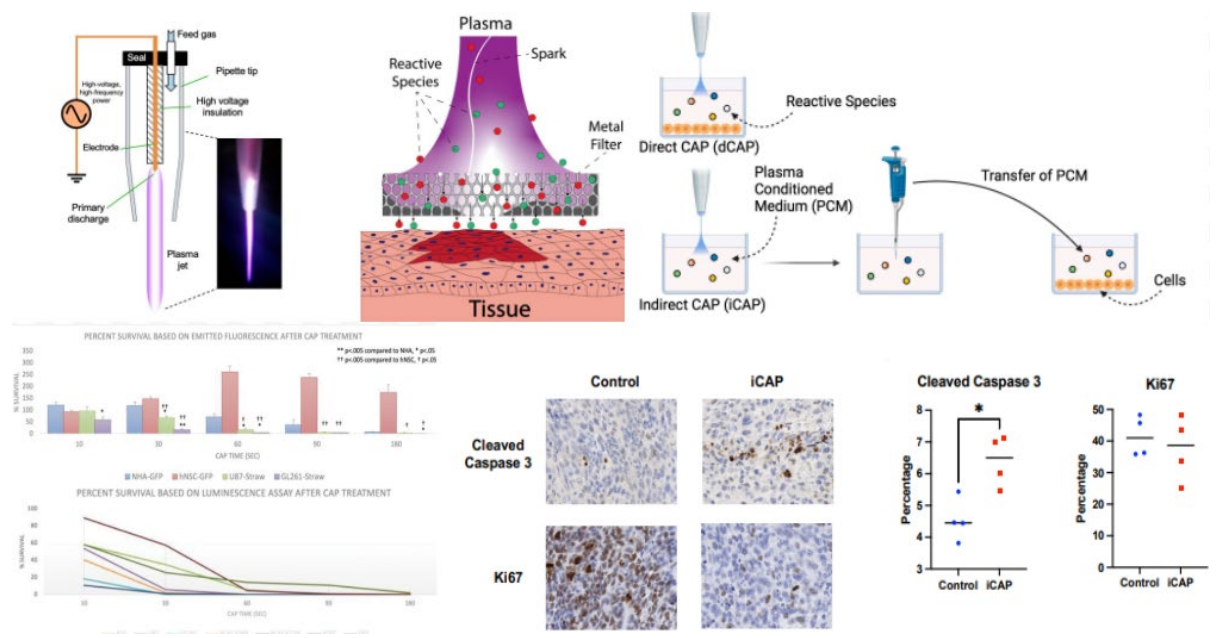


Figure 18. Cold atmospheric plasma (CAP) and its plasma-material interactions are illustrated. Upper left shows a diagram and image of the plasma jet in operation. Middle right presents a diagram of a porous aluminum VCM filtering sparks while delivering CAP. Upper right outlines two delivery methods: Direct CAP, where both cells and culture medium are exposed to CAP, and Indirect CAP, where only the culture medium is exposed to CAP before being transferred to a cell-containing well. Bottom left demonstrates tumor selectivity in glioma-engrafted cerebral organoid material, with CAP preferentially killing rapidly dividing cells (top) while normal neural cell lines, such as human astrocytes and differentiated human fetal neural stem cells, exhibit significant resistance to cell death. Middle bottom features representative IHC images of xenograft tumors for cleaved Caspase-3 and Ki67. Bottom right shows the percentage staining for Caspase-3 and Ki67 in CAP and control groups, with significance noted (*: p < 0.05).

Acknowledgments

Research performed at the Plasma, Energy, & Space Propulsion Laboratory has been funded by a variety of sources including the Air Force Research Lab, the Joint Advanced Propulsion Institute (NASA Grant No. 80NSSC21K1118), other NASA funding, the Air Force Office of Scientific Research (AFOSR Award No. FA9550-25-1-0012), the US Department of Energy, Advanced Research Projects Agency-Energy, the Office of Science–Fusion Energy Sciences, and others.

References

¹Eric A Viges, Benjamin A Jorns, Alec D Gallimore, and JP Sheehan. University of Michigan's upgraded large vacuum test facility. In 36th International Electric Propulsion Conference, pages 1–18, 2019

²Richard A. Obenchain, Ehsan E. Taghizadeh, and Richard E. Wirz. Collisionless flux-based analyses of neutral drift and transport in hall thruster test facilities. In 39th International Electric Propulsion Conference, pages IEPC–2025–606, 2025.

³Richard A. Obenchain, Tyler Topham, Sophia Bergmann, John Foster, and Richard E. Wirz. Charge exchange (cex) corrections for electric propulsion facilities. In 39th International Electric Propulsion Conference, pages IEPC–2025–609, 2025



- ⁴Tyler Topham. Understanding the Mechanisms Affecting Gridded Ion Engine Operation in Ground Test Facilities. PhD thesis, University of Michigan, 2025.
- ⁵Cretel, C. M. and Wirz, E. R., (2025). *Electric Propulsion Mission Optimization using Reduced Order Models*, International Electric Propulsion Conference, London, UK. (IEPC-25-585)
- ⁶Breddan, Mckenna & Wirz, Richard. (2025). Plume divergence characterization for electric propulsion via standard deviation and emittance. Journal of Electric Propulsion. 4. 10.1007/s44205-025-00113-5. http://dx.doi.org/10.1007/s44205-025-00113-5
- ⁷1S. P. Berg and J. L. Rovey, "Assessment of Multimode Spacecraft Micropropulsion Systems," Journal of Spacecraft and Rockets, vol. 54, no. 3, pp. 592–601, Mar. 2017, publisher: American Institute of Aeronautics and Astronautics. https://doi.org/10.2514/1.A3364
- ⁸ J. L. Rovey, C. T. Lyne, A. J. Mundahl, N. Rasmont, M. S. Glascock, M. J. Wainwright, and S. P. Berg, "Review of multimode space propulsion," Progress in Aerospace Sciences, vol. 118, p. 100627, Oct. 2020.https://www.sciencedirect.com/science/article/pii/S0376042120300397
- ⁹3S. Parmar, O. Cohen, K. Persson, J. Mcdaniel, G. Vaghjiani, and R. Wirz, "Multimode Propellant Discovery: A Computational High-throughput Screening Paradigm," in The 38th International Electric Propulsion Conference, Toulouse, France, 2024.
- ¹⁰ S. M. Parmar, D. D. Depew, R. E. Wirz, and G. L. Vaghjiani, "Structural Properties of HEHN- and HAN-Based Ionic Liquid Mixtures: A Polarizable Molecular Dynamics Study," The Journal of Physical Chemistry B, vol. 127, no. 40, pp. 8616–8633, Oct. 2023, publisher: American Chemical Society. https://doi.org/10.1021/acs.jpcb.3c02649
- T. Enomoto, S. M. Parmar, R. Yamada, R. E. Wirz, and Y. Takao, "Molecular Dynamics Simulations of Ion Extraction from Nanodroplets for Ionic Liquid Electrospray Thrusters," Journal of Electric Propulsion, vol. 1, no. 1, p. 13, 2022. https://doi.org/10.1007/s44205-022-00010-1
- ¹² D. D. Depew, G. L. Vaghjiani, S. M. Parmar, and J. J. Wang, "Liquid Structure and Hydrogen Bonding in Aqueous Hydroxylammonium Nitrate," The Journal of Physical Chemistry B, vol. 128, no. 3, pp. 824–840, Jan. 2024, publisher: American Chemical Society. https://doi.org/10.1021/acs.jpcb.3c05623
- ¹³ B. D. Rabideau, M. Soltani, R. A. Parker, B. Siu, E. A. Salter, A. Wierzbicki, K. N. West, and J. H. Davis, "Tuning the melting point of selected ionic liquids through adjustment of the cation's dipole moment," Physical Chemistry Chemical Physics, vol. 22, no. 21, pp. 12301–12311, 2020, publisher: The Royal Society of Chemistry. http://dx.doi.org/10.1039/D0CP01214A
- ¹⁴ R. K. Blundell and P. Licence, "Tuning cation–anion interactions in ionic liquids by changing the conformational f lexibility of the cation," Chemical Communications, vol. 50, no. 81, pp. 12080–12083, 2014, publisher: The Royal Society of Chemistry. http://dx.doi.org/10.1039/C4CC05505E
- ¹⁵ A. Jain, S. P. Ong, G. Hautier, W. Chen, W. D. Richards, S. Dacek, S. Cholia, D. Gunter, D. Skinner, G. Ceder, and K. A. Persson, "Commentary: The Materials Project: A materials genome approach to accelerating materials innovation," APL Materials, vol. 1, no. 1, p. 011002, Jul. 2013. Available: https://doi.org/10.1063/1.4812323
- ¹⁶ A. M. Ganose, H. Sahasrabuddhe, M. Asta, K. Beck, T. Biswas, A. Bonkowski, J. Bustamante, X. Chen, Y. Chiang, D. C. Chrzan, J. Clary, O. A. Cohen, C. Ertural, M. C. Gallant, J. George, S. Gerits, R. E. A. Goodall, R. D. Guha, G. Hautier, M. Horton, T. J. Inizan, A. D. Kaplan, R. S. Kingsbury, M. C. Kuner, B. Li, X. Linn, M. J. McDermott, R. S. Mohanakrishnan, A. N. Naik, J. B. Neaton, S. M. Parmar, K. A. Persson, G. Petretto, T. A. R. Purcell, F. Ricci, B. Rich, J. Riebesell, G.-M. Rignanese, A. S. Rosen, M. Scheffler, J. Schmidt, J.-X. Shen, A. Sobolev, R. Sundararaman, C. Tezak, V. Trinquet, J. B. Varley, D. Vigil-Fowler, D. Wang, D. Waroquiers, M. Wen, H. Yang, H. Zheng, J. Zheng, Z. Zhu, and A. Jain, "Atomate2: modular workflows for materials science," Digital Discovery, Jul. 2025, publisher: RSC. https://pubs.rsc.org/en/content/articlelanding/2025/dd/d5dd00019j
- ¹⁷ S. P. Ong, W. D. Richards, A. Jain, G. Hautier, M. Kocher, S. Cholia, D. Gunter, V. L. Chevrier, K. A. Persson, and G. Ceder, "Python Materials Genomics (pymatgen): A robust, open-source python library for materials analysis," Computational Materials Science, vol. 68, pp. 314–319, 2013. https://www.sciencedirect.com/science/article/pii/S0927025612006295
- ¹⁸ A. S. Rosen, M. Gallant, J. George, J. Riebesell, H. Sahasrabuddhe, J.-X. Shen, M. Wen, M. L. Evans, G. Petretto, D. Waroquiers, G.-M. Rignanese, K. A. Persson, A. Jain, and A. M. Ganose, "Jobflow: Computational Workflows Made Simple," Journal of Open Source Software, vol. 9, no. 93, p. 5995, 2024.



- ¹⁹ A. Jain, S. P. Ong, W. Chen, B. Medasani, X. Qu, M. Kocher, M. Brafman, G. Petretto, G.-M. Rignanese, G. Hautier, D. Gunter, and K. A. Persson, "FireWorks: a dynamic workflow system designed for high-throughput applications," Concurrency and Computation: Practice and Experience, vol. 27, no. 17, pp. 5037–5059, Dec. 2015, publisher: John Wiley & Sons, Ltd. https://doi.org/10.1002/cpe.3505
- ²⁰ S. V. Sambasivarao and O. Acevedo, "Development of OPLS-AA Force Field Parameters for 68 Unique Ionic Liquids," Journal of Chemical Theory and Computation, vol. 5, no. 4, pp. 1038–1050, Apr. 2009, publisher: American Chemical Society. https://doi.org/10.1021/ct900009a
- ²¹ J. G. McDaniel, E. Choi, C. Y. Son, J. R. Schmidt, and A. Yethiraj, "Ab Initio Force Fields for Imidazolium-Based Ionic Liquids," The Journal of Physical Chemistry B, vol. 120, no. 28, pp. 7024–7036, 7 2016. https://doi.org/10.1021/acs.jpcb.6b05328
- ²² Y. Wang, J. Fass, and J. D. Chodera, "End-to-End Differentiable Molecular Mechanics Force Field Construction," ArXiv, vol. abs/2010.0, 2020
- ²³ Chabert P., Arancibia Monreal, J., Bredin, J., Popelier, L. and Aanesland, A., "Global model of a gridded-ion thruster powered by a radiofrequency inductive coil," Physics of Plasmas, Vol. 19, No. 7, pp. 073512, 2012.
 - ²⁴ Chabert P, Braithwaite N. Physics of Radio-Frequency Plasmas. Cambridge University Press; 2011
- ²⁵ Chaplin, V.H., Johnson, L.K., Lobbia, R.B., Konopliv, M.F., Simka, T. and Wirz, R.E., "Insights from Collisional-Radiative Models of Neutral and Singly Ionized Xenon in Hall Thrusters," Journal of Propulsion and Power, Vol. 38, No. 5, pp. 866-879, 2022.
- ²⁶ Crandall P., Wirz, R.E., 2024. Miniature RF Gridded Ion Thruster For Air-Breathing EP, IEPC, Toulouse, France. (IEPC-2024-259)
- ²⁷ Konopliv, M. F., Wirz, R. E., and Johnson, L. K., "Ion-Neutral Population and Electron Temperature Phasing in the Hall Thruster Breathing Mode," *IEPC*, Toulouse, France, 2024. (IEPC-2024-487).
- ²⁸ Mary F. Konopliv, Lee K. Johnson, Richard E. Wirz; Time-resolved electron temperature oscillations in Hall thrusters. *J. Appl. Phys.* 28 June 2025; 137 (24): 243303. https://doi.org/10.1063/5.0255921
- ²⁹ Harteloo, A. M. and Wirz, R. E., (2025) *Broadband Characterization of Hall Thruster Discharge and Cathode Multimode Plasma Oscillations via FastOES*, IEPC, London, UK. (IEPC-2025-665)
- ³⁰ Konopliv, M, and Wirz, R. E., (2024) *Cathode Species Contributions to Hall Thruster Plume* Dynamics, IEPC, Toulouse, France. (IEPC-2024-488)
- ³¹ Hofbeck, I. J. and Wirz, R. E., (2025) *Spatial Spectroscopy for Hall Thruster Plume Species*, IEPC, London, UK. (IEPC-25-630).
 - ³² Chen, F., 1992. Capacitor Tuning Circuits for Inductive Loads. (Report)
- ³³ Piejak, R.B., Godyak, V.A., Alexandrovich, B.M., 1992. A simple analysis of an inductive RF discharge. PSST. 1, 179–186.
- ³⁴ Franz, L. K. and Wirz, R., "Xe-C Scattering, Implantation, and Sputtering Analysis for EP Systems," *38th International Electric Propulsion Conference*, 2024, pp. IEPC–2024–552
- ³⁵ Eckstein, W. "Computer Simulation of Ion-Solid Interactions," *Springer-Verlag*, Springer Series in Materials Science. 1991
- ³⁶ Biswas, S., Obenchain, R. A., Cowan, R. W., and Wirz, R. E., "Review of PMI data for HET-induced erosion of facility surfaces," 38th International Electric Propulsion Conference, 2024, pp. IEPC–2024–532.
- ³⁷ Cabrera et al. Pressure Facility Effects on the Impedance Characteristics of a 9-kW HET. In 38th International Electric Propulsion Conference, pages IEPC-2024-808, 2024
- ³⁸ Tartz, M., & Neumann, H. (2007). Sputter yields of carbon materials under xenon ion incidence. *Plasma Processes and Polymers*, 4(S1). https://doi.org/10.1002/ppap.200731502
- ³⁹ R. Deltschew, M. Tartz, V. Plicht, E. Hartmann, H. Neumann, Sputter Characteristics of Carbon-Carbon Compound Material. 27th International Electric Propulsion Conference, 2001
- ⁴⁰ Cowan R.W., Biswas, S., Franz, L.K., Cretel, C.M., Obenchain, R.A., Wirz, R.E., Hall thruster krypton sputtering and deposition for vacuum facility materials. J Electric Propulsion 4, 45 (2025). https://doi.org/10.1007/s44205-025-00142-0
- ⁴¹ Kolasinski, R. D., Polk, J. E., Goebel, D., & Johnson, L. K. (2008). Carbon sputtering yield measurements at grazing incidence. Applied Surface Science, 254(8), 2506–2515. doi:10.1016/j.apsusc.2007.09.082
 - ⁴² G. K. Wehner, General Mills Report No. 2309 (1962)



- ⁴³ D. Rosenberg and G. K. Wehner. Sputtering yields for low energy he+, kr+, and xe+ ion bombardment. Journal of Applied Physics, 33(5):1842–1845, 1962. Published by the American Institute of Physics.
- ⁴⁴ E. Hecht and J. Bohdansky. Sputtering behavior of graphite and molybdenum at low bombarding energies. Journal of Nuclear Materials, 122 and 123:1431–1436, 1984.
- ⁴⁵ R. Deltschew, M. Tartz, V. Plicht, E. Hartmann, H. Neumann, H. J. Leiter, and J. Esch. Sputter yield measurements of graphite and carbon-carbon material for ion thruster grids. In 37th AIAA/ASME/SAE/ASEE Joint Propulsion
- ⁴⁶ Williams, J., Johnson, M., & Williams, D. (2004). Differential sputtering behavior of pyrolytic graphite and carbon-carbon composite under Xenon bombardment. *40th AIAA/ASME/SAE/ASEE Joint Propulsion Conference and Exhibit*. https://doi.org/10.2514/6.2004-3788
- ⁴⁷ Tran, H. D., Clark S. A., Thompson, R., Levin, De. A., Rovey, J. L., & Chew, H. B. (2024). Carbon Transport in Electric Propulsion Testing–I: Multiscale Computations for Carbon Sputtering by Low Energy Ion Bombardment. In *AIAA SCITECH 2024 Forum (P. 1135*).
- ⁴⁸ Li, G. Z. and Wirz, R. E., "Persistent sputtering yield reduction in plasma-infused foams," Physical Review Letters, Vol. 126, No. 3, 2021, pp. 035001.
- ⁴⁹ Graeme Sabiston, Richard E. Wirz; Ion–surface interactions in plasma-facing material design. *J. Appl. Phys.* 14 May 2024; 135 (18): 183301. https://doi.org/10.1063/5.0201758
- ⁵⁰ Sabiston, G. T. and Wirz, R. E., "Thrust Densification of Space Electric Propulsion Systems via Volumetrically Complex Materials," *AIAA SCITECH 2024 Forum*, 2024, p. 1136.
- 51 Sabiston, G. and Wirz, R. E., "Electric Propulsion Vacuum Chamber Design Approaches for Reducing Sputtering Effects," 38th International Electric Propulsion Conference, 2024, pp. IEPC–2024–187.
- ⁵² Fernandez-Coppel, Jorge, Richard Wirz, and Jaime Marian. "Fully discrete model of kinetic ion-induced electron emission from metal surfaces." *Journal of Applied Physics* 135.8 (2024).
- ⁵³ Fernandez-Coppel, Jorge, Richard E. Wirz, and Jaime Marian. "Analytical quantum model of potential electron emission from metal surfaces by low-energy noble gas ions." *Applied Surface Science* (2025): 163251.
- ⁵⁴ H.-Y. Chang, A. Alvarado, and J. Marian, "Calculation of secondary electron emission yields from low-energy electron deposition in tungsten surfaces," Appl. Surf. Sci. 450, 190–199 (2018).
- ⁵⁵ H.-Y. Chang, A. Alvarado, T. Weber, and J. Marian, "Monte Carlo modeling of low-energy electron-induced secondary electron emission yields in micro-architected boron nitride surfaces," Nucl. Instrum. Methods Phys. Res. Sec. B 454, 14–22 (2019).
- ⁵⁶ Haist, B.; Wirz, R.E. Network Analysis as a Method for Identifying Operational Modes of Cold Atmospheric Plasma Jets. *Plasma* **2025**, *8*, 10. https://doi.org/10.3390/plasma8010010
- ⁵⁷ Chen, Z. and Wirz, R. E., Cold atmospheric plasma (CAP) technology and applications, Morgan & Claypool Publishers, 2021.
- ⁵⁸ Chen, Z., Garcia, G., Arumugaswami, V., and Wirz, R. E., "Cold atmospheric plasma for SARS-CoV-2 inactivation," Physics of Fluids, Vol. 32, No. 11, 2020.
- ⁵⁹ Chen, Z., Bai, F., Jonas, S. J., and Wirz, R. E., "Cold atmospheric plasma for addressing the COVID-19 pandemic," Plasma Processes and Polymers, Vol. 19, No. 9, 2022, pp. 2200012.
- ⁶⁰ Chen, G., Chen, Z., Wang, Z., Obenchain, R., Wen, D., Li, H., Wirz, R. E., and Gu, Z., "Portable air-fed cold atmospheric plasma device for postsurgical cancer treatment," Science Advances, Vol. 7, No. 36, 2021, pp. eabg5686.
- ⁶¹ Chen, Z., Chen, G., Obenchain, R., Zhang, R., Bai, F., Fang, T., Wang, H., Lu, Y., Wirz, R. E., and Gu, Z., "Cold atmospheric plasma delivery for biomedical applications," Materials Today, Vol. 54, 2022, pp. 153.
- ⁶² Zhitong Chen, Richard Obenchain, Richard E. Wirz, "Cold plasma treatment for biomedical applications: using aluminum foam to reduce risk while increasing efficacy," arXiv preprint arXiv:2305.18349 (2023).
- ⁶³ Ottaviano, A., & Wirz, R. E., "Secondary electron emission of reticulated foam materials," Journal of Applied Physics, 133(10) (2023).

